CMES: Computer Modeling in Engineering and Sciences, Vol. 37, No. 1, pp 1-23, 2008

Insight into High-quality Aerodynamic Design Spaces through Multi-objective Optimization

T. Kipouros[1], D.M. Jaeggi[2], W.N. Dawes[3], G.T. Parks[2], A.M. Savill[4] and P.J. Clarkson[2]

Abstract: An approach to support the computational aerodynamic design process is presented and demonstrated through the application of a novel multi-objective variant of the Tabu Search optimization algorithm for continuous problems to the aerodynamic design optimization of turbomachinery blades. The aim is to improve the performance of a specific stage and ultimately of the whole engine. The integrated system developed for this purpose is described. This combines the optimizer with an existing geometry parameterization scheme and a well-established CFD package. The system's performance is illustrated through case studies – one two-dimensional, one three-dimensional – in which flow characteristics important to the overall performance of turbomachinery blades are optimized. By showing the designer the trade-off surfaces between the competing objectives, this approach provides considerable insight into the design space under consideration and presents the designer with a range of different Pareto-optimal designs for further consideration. Special emphasis is given to the dimensionality in objective function space of the optimization problem, which seeks designs that perform well for a range of flow performance metrics. The resulting compressor blades achieve their high performance by exploiting complicated physical mechanisms successfully identified through the design process. The system can readily be run on parallel computers, substantially reducing wall-clock run times – a significant benefit when tackling computationally demanding design problems. Overall optimal performance is offered by compromise designs on the Pareto trade-off surface revealed through a true multi-objective design optimization test case. Bearing in mind the continuing rapid advances in computing power and the benefits discussed, this approach brings the adoption of such techniques in real-world engineering design practice a step closer.

keyword: Multi-objective optimization, design optimization modeling, metaheuristic continuous optimization, Tabu Search, aerodynamic design, turbomachinery, parallel computing.

1 Introduction

Substantial progress has been made in computational aerodynamic design in both academia and industry in the past decade [Keane and Nair (2005)]. Simultaneously, closely related general design methodologies have influenced a wide range of disciplines and applications, promoting the use of optimization as an enabling technology in technological innovation [Vanderplaats (2001)], while the rapid evolution of computing technology has facilitated the use of optimization in design in a real-world framework [Kroo (2004)]. Multi-objective and multi-disciplinary optimization tools are increasingly important to the design process for many real-world applications [Deb (2001); Alexandrov (2005)]. These tools have the potential both to reduce substantially the length of the design cycle and to improve the quality of the designed product. In the engineering context, the large size and complex nature of the field of aerodynamics presents some of the toughest, most demanding design optimization problems.

The industrial and academic aeronautical design communities have invested much effort in the development of sophisticated automated integrated multi-disciplinary aerodynamic design optimization systems [Keane and Nair (2005)]. Extensive computational optimization is becoming an ever more realistic prospect thanks to the inexorable improvements in raw computing power available allied to continuing developments in optimizers, in analysis tools, in new surrogate modeling tools, and in post-optimization analysis techniques [Lian and Liou (2005);

[1] Applied Mathematics and Computing, School of Engineering, Cranfield University, UK.
[2] Engineering Design Centre, Department of Engineering, University of Cambridge, UK.
[3] Computational Fluid Dynamics Laboratory, Department of Engineering, University of Cambridge, UK.
[4] Computational Aerodynamic Design, School of Engineering, Cranfield University, UK.

Kipouros, Mleczko, and Savill (2008)]. Moreover, improvements in parameterization and representation techniques help by reducing the number of design variables needed and thus the dimensionality of the design space to be searched, but still allow complex 3D geometry to be captured accurately.

The optimization of airfoil designs is typical of aerodynamic design problems in general in that it is a challenging, computationally expensive, highly constrained, nonlinear problem. In consequence, the use of non-gradient optimization algorithms is essential [Hajela (1999)]. Heuristic search techniques have a clear role in handling design optimization problems with non-convex or disjoint design spaces with continuous design variables. As with most real-world problems, there are multiple (usually conflicting) performance metrics that an engineer might seek to improve in optimizing, for example, the design of turbomachinery blades. This suggests a multi-objective approach, a notion that is reinforced by the recognition that any consideration of robustness – the retention of performance over a range of operating conditions, in the face of geometry changes (e.g. through creep) etc. – must also inevitably entail multiple objectives.

The evolution and future direction of the design process for one particular aerodynamic application – the design of compressors – has been reviewed recently by Molinari and Dawes (2006). They conclude that, with technology development in turbomachinery design having almost reached an asymptote, the new challenge is to develop new design tools and methodologies that enable current technology to be applied faster and more reliably. To meet the objectives set by the Advisory Council for Aeronautics Research in Europe [ACARE (2002, 2004)] – to generate innovative and affordable solutions and, fundamentally, to push past the asymptote for the current generation of large civil jet engines – they suggest that computational fluid dynamics (CFD) tools should be more highly integrated in the design process by making them fully available from the preliminary analysis stage. The use of multi-objective search methods is particularly appropriate in the early stages of the design process when it is most natural to explore the trade-offs available between competing concepts.

Some recent studies have embraced multi-objective optimization in aerodynamic design and show the possible benefits compared to single-objective optimization with a composite objective function. In one of the earliest examples of such an application, Sasaki, Obayashi, and Nakahashi (2002) combined a genetic algorithm (GA) with a Navier-Stokes code to optimize the design of wings for a supersonic transport aircraft.

Gaiddon, Knight, and Poloni (2004) performed multi-objective optimization on a supersonic missile inlet. They compared a number of optimization algorithms using both composite and multiple objective functions, and concluded that "performing real multiobjective optimization and finding a Pareto front is the only effective way to find a set of designs satisfying several performance criteria in an industrial context."

Nemec, Zingg, and Pulliam (2004) performed multi-objective optimization on both a single and a multi-element 2-D aerofoil. Their integrated approach combined a Newton-Krylov adjoint CFD code, a b-splines-based parameterization scheme, and both a gradient-based optimizer and a GA. They obtained encouraging results on some simple test problems.

Chiba, Obayashi, Nakahashi, and Morino (2005) optimize the design of the wings of a transonic regional jet aircraft from a multi-objective, multi-disciplinary perspective. This is a large-scale, real-world application with aerodynamic, structural and aeroelasticity objectives using high-fidelity evaluation models. The system used exploits parallel processing and the same GA-based optimizer developed and described by Sasaki, Obayashi, and Nakahashi (2002).

Amirante, Catalano, Dadone, and Daloiso (2007) carried out single-objective optimization of the intake of a real small-scale turbojet engine using a gradient-based progressive optimization technique. They achieved satisfactory improvements in the performance of the engine and validated the results experimentally. However, they recognize the value of multi-objective optimization and suggest extending their approach to a multi-point optimization problem by deploying the auto-adjusting weighted formulation of the objective function proposed by Zhu, Liu, Wang, and Yu (2004).

This paper describes the development of an automatic integrated design system for multi-objective aerodynamic design optimization problems. This system is specifically developed for real turbomachinery applications, and its performance is examined through a single-row stator compressor test case. The aims of the research are

to improve the performance of this specific stage, and ultimately that of the whole engine, and to demonstrate how the combined use of CFD and a suitably adapted multi-objective optimizer can significantly enhance the design process, not only in terms of design quality but also in terms of the insight into the nature of the design space afforded to the designer. Furthermore, we highlight the need to tailor the computational tools to the nature of the specific design process under investigation, in order to exploit fully the potential of the available computational engineering design technology. This is reinforced by the approach and methodology proposed by Morino, Bernardini, and Mastroddi (2006) for the multi-disciplinary design of aircraft configurations. The optimization modeling is crucial in multi-disciplinary design problems, where design parameters and objectives exhibit different natural characteristics. The electromechanical design problem presented in Jimenez-Octavio, Lopez-Garcia, Pilo, and Carnicero (2008) successfully demonstrates and validates this notion in a different application domain.

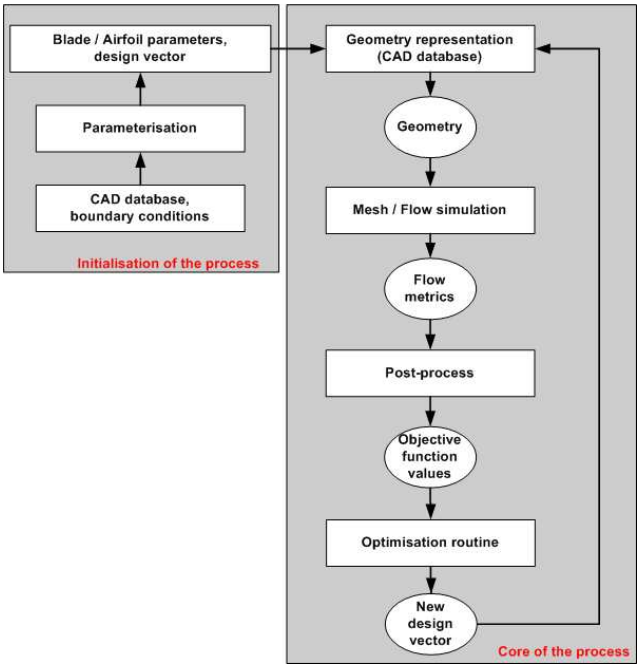


Figure 1 : The basic steps of an integrated computational aerodynamic design optimization system

2 Overview of the blade optimization system

The system, Multi-Objective Blade Optimization System in 3 Dimensions (MOBOS3D), used in this work has been developed and described by Kipouros, Parks, Savill, and Jaeggi (2004) building on the single-objective integrated design optimization system BOS3D developed by Harvey (2002) and described by Dawes, Kellar, Harvey, Dhanasekaran, Savill, and Cant (2003). The system combines an existing, efficient and flexible geometry parameterization scheme, a well-established CFD package and a novel multi-objective variant of the Tabu Search (TS) optimization algorithm for continuous problems [Jaeggi, Parks, Kipouros, and Clarkson (2006)].

Fig. 1 presents a flow diagram showing the stages of the process executed by MOBOS3D. The first stage is the parameterization of the initial blade design, input through an initial CAD geometry, together with boundary conditions for the flow solution. This is an important stage of the process in which the long and complicated CAD file description is transformed into a short, manageable string of numbers – the design vector. The geometry is parameterised using a Partial Differential Equation (PDE) approach [Bloor and Wilson (1995)], giving a compact but flexible representation of the design, in a design vector comprising 26 variables. This design vector is the input to the main loop of the design system, which consists of the flow simulation and optimization processes.

Harvey (2002) undertook detailed investigations, for the design problem in question, in order to identify the most appropriate choice from the available techniques for each stage of the system. Geometrical modeling in an automated manipulation (conversion from CAD to CFD formats) is a quite time-consuming activity and a serious obstacle to design optimization of aerodynamic forms [Dawes, Kellar, Harvey, Dhanasekaran, Savill, and Cant (2003)]. It may be preferable to use parameters that maximize geometrical flexibility rather than those most familiar to the human designer. In this context, the PDE method, described by Bloor and Wilson (1995), was found by Harvey to offer an exceptional level of geometrical flexibility.

On receipt of a new design vector, a computational mesh is automatically generated from the geometry specification, and then a detailed CFD analysis (blade to blade) is performed. The mesh is a 3D H-type structured grid consisting of $31\times97\times45$ nodes in each direction (tangential, axial, radial). The flow simulation is performed by the BTOB3D CFD code solving the 3D Navier-Stokes equations. This routine returns all the metrics needed

to describe the flow around the blade [Dawes (1988)]. The generality and robustness of the CFD code has been extensively demonstrated by application to a variety of test cases in industry and academia. It is essential to use a Reynolds-Averaged Navier-Stokes (RANS) solver because, in order to improve the blade design, accurate predictions of the complicated viscous flow in the compressor are required, especially to capture the secondary flow effects responsible for the profile and endwall losses. Based on this simulation, the objective functions and constraints are evaluated and the optimizer then generates new design vectors that are, in turn, meshed and evaluated. This process continues until a termination criterion is met.

Heuristic optimization methods have been found to be effective in tackling aerodynamic shape design problems, and (near-)optimal solutions within relatively complex design spaces can be located in a reasonable amount of computation time [Aly, Ogot, and Pelz (1996)]. Gradient-based optimization schemes tend to get trapped in the numerous real and false local minima common in the design spaces of real-world aerodynamic applications. The most widely used heuristic algorithms are Simulated Annealing (SA) [Kirkpatrick, Gelatt, and Vecchi (1983), Aarts and Korst (1989)], Genetic Algorithms (GA) [Goldberg (1989)] and Tabu Search (TS) [Glover and Laguna (1997)]. TS is relatively simple to implement and has been shown to have great potential in the field of aerodynamics [Harvey (2002)]. The choice of TS does not imply that it is in general superior to the SA and GA methods in optimizing aerodynamic problems. It is simply argued that TS has been shown to be particularly effective in this application domain, and hence it is likely to perform well in the context of this research.

At the end of the optimization process, the best design vectors identified and their associated flow solutions are converted into a single output file. This is accomplished by using Non-Uniform Rational B-Splines (NURBS) [Rogers (2000)], a representation technique appropriate for complex 3D reconstructions, approximating curves well using a small number of control points. The optimal geometries can then be examined in detail through, for instance, contour plots.

The system is parallelized by means of functional decomposition using the Message Passing Interface (MPI) protocol [Snir, Otto, Huss-Lederman, Walker, and Dongarra (1998)]. The new design vectors generated by the optimizer are sent to the slaves of a cluster for CFD evaluation. Then, the flow metrics of each new blade are returned to the master of the cluster, which controls the optimization process.

3 Definition and evaluation of objectives and constraints

3.1 Feasibility of designs

Even though the parameterization scheme used in MOBOS3D is very flexible, at the same time a drawback arises: the possibility of generating infeasible geometries. When using traditional engineering design parameters it is often built into the blade representation that thickness is guaranteed to be positive, that the leading edge (LE) has a certain minimum radius and that the blade fits between adjacent rows. In MOBOS3D, until the mesh generation process begins, it is not possible to give the same assurances by inspecting the blade's design vector in PDE parameter form. This adds a layer of complexity to the management of the geometry and its physical feasibility, but it is a price worth paying for the additional flexibility, and hence scope for considering more innovative designs, associated with the PDE-based representation.

Similar complexities are imposed on the design process when considering the physical or designer-defined aerodynamic feasibility of new blade shapes. A particular design can cause flow patterns that are physically unacceptable, but it is also possible for the numerical flow solver to fail to produce a converged flow solution for certain designs. Thus, new candidate designs could be infeasible for geometric, aerodynamic or computational reasons. In all these cases, infeasibility is treated as a hard constraint. In practice it is found that much of the available search space in this application is infeasible [Molinari, Jarrett, Clarkson, and Dawes (2006)].

3.2 Definition and modeling of the objective flow metrics

In previous studies, blockage, the extent to which viscous forces restrict the effective flow area in a blade passage, and entropy generation rate, an overall measure of losses associated with the design, were used as objectives [Kipouros, Jaeggi, Dawes, Parks, Savill, and Clarkson (2008)]. In order to explore in more detail the way in which blade design affects the mechanisms of loss gen-

eration, here mass-averaged profile and endwall losses along the span of the blade in the wake region of the flow are extracted from the flow solution and used as objectives.

3.2.1 Blockage

Blockage is an estimation of the amount of low momentum mass flow in the vicinity of the hub and tip regions, or the stage inefficiency. Exact measures of loss from CFD are unreliable, so the use of velocity to measure performance has considerable attraction. The formula used here to compute blockage was developed by Harvey, Dawes, and Gallimore (2003) as a heuristic assessment of the magnitude of "bad flow features" and is encoded as

$$\begin{cases} V_{low} = \frac{8}{10} min(V) + \frac{2}{10} max(V) \\ V_{high} = \frac{9}{10} max(V) + \frac{1}{10} min(V) \end{cases} \tag{1}$$

$$B = \frac{\int\limits_A \left(V_{high} - min\left[V_{high}, max[V_{low}, V]\right]\right) dA_x}{\int\limits_A dA_x} \tag{2}$$

where V is the magnitude of fluid velocity.

Eq. 1 sets up limiting velocities to moderate any extrema, or spikes, which can appear in the flow solution, and the integral in Eq. 2 is executed over a mesh quasi-orthogonal (r-θ) plane, A. Usually A lies halfway between the trailing edge (TE) and the exit plane, to allow some boundary layer development, but not the total smearing out of any secondary flows.

3.2.2 Secondary Losses

A key precursor for future improvements in turbomachinery designs is a detailed understanding of loss generation in the presence of the unsteady effects induced by the machine environment. Better understanding of loss mechanisms, and thus of general flow characteristics, is essential for the optimization of turbomachines, particularly at off-design conditions, and in the unsteady flow prevailing in multi-blade row machines. Achieving high efficiency and operating stability in off-design conditions depends on the control of loss mechanisms and small scale flows in the compressors [Haller, Walker, Singh, and Inche (1997)]. Detailed explanations of the theory and the importance of these losses can be found in Storer and Cumpsty (1991), Denton (1993) and Dunham (1995).

The secondary flows along the span of the compressor blade, arising from the interaction of the endwall boundary layers and the blade passage, and tip clearance flows, are principally responsible for the development of the secondary losses. Mass-averaged pressure losses are defined and modeled in order to examine the effects of these complex aerodynamic phenomena. An accurate 3D RANS CFD code is required to capture the detailed flow characteristics.

First, a non-dimensional stagnation pressure is defined:

$$p_{stag} = \frac{p/T^{\frac{\gamma}{\gamma-1}}}{p_0/T_0^{\frac{\gamma}{\gamma-1}}} \tag{3}$$

This takes values between 0 and 1, and implies no losses when it takes the highest value (for an isentropic process). The 0 subscripts denote the stagnation conditions in the mid-span position at the inlet of the passage. Then the mass-averaged stagnation pressure along the passage can be defined as:

$$\overline{p_{stag}} = \frac{\int\limits_A \dot{m} p_{stag} dA}{\int\limits_A \dot{m} dA} \tag{4}$$

where $\dot{m}$ is the mass flow rate through the passage. Finally, the loss coefficient is described by:

$$C_{loss} = \frac{\Delta\overline{p_{stag}}}{p_0 - p_{inlet}} \tag{5}$$

where p_{inlet} denotes the average static pressure on the mid-span (x-θ) plane at the inlet of the stator row.

The datum blade geometry, shown in Fig. 2, has been considered during the development of these flow metrics. The conventional and uniform shape of this blade facilitates the verification of the implementation of the mass-averaged pressure loss calculations, since the behavior of the flow around similar geometries can be predicted from experience.

The mass-averaged pressure losses along the passage are shown in Fig. 3. The predicted losses follow the expected behavior, and the position of the blade in the axial direction of the passage is clearly recognizable. The grid has an axial dimension of 97, and the trailing edge of the blade lies on the 72nd r-θ plane, followed by the viscous wake.

Fig. 4 presents the mass-averaged pressure loss distribution along the span of the blade (radial direction) for different axial positions. The blade span fraction shown on

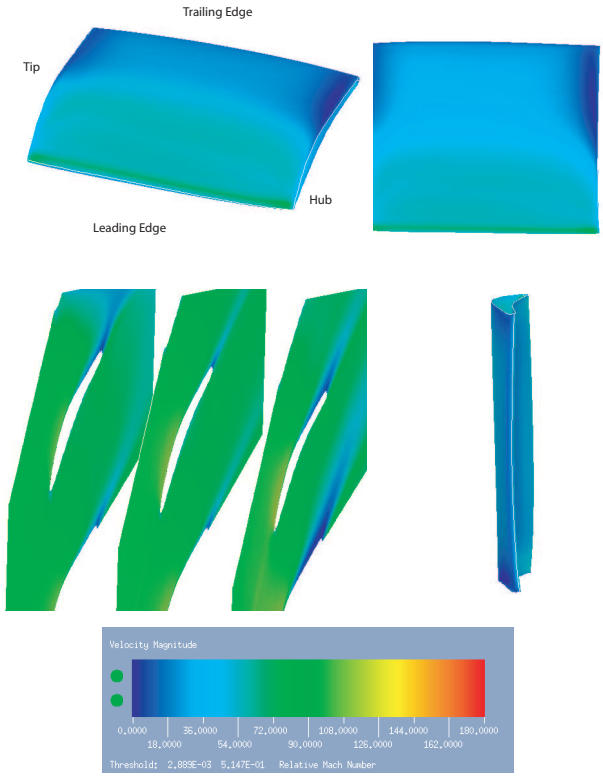


Figure 2 : The datum blade geometry showing its velocity magnitude distribution; top left: 3D view; top right: suction side normal view; bottom left: 2D profiles on hub / midspan / tip regions; bottom right: downstream side view

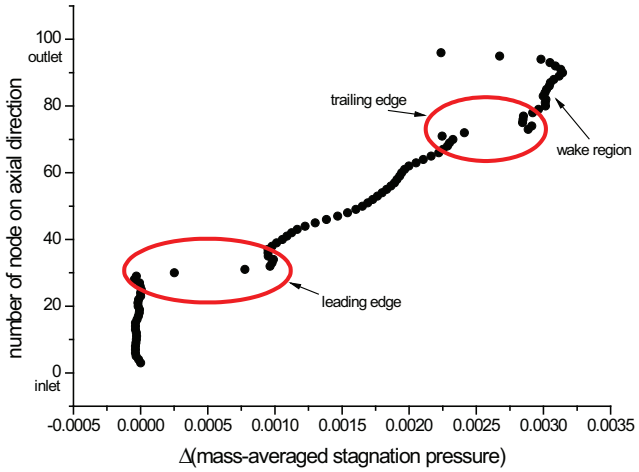


Figure 3 : Mass-averaged pressure losses along the flow passage

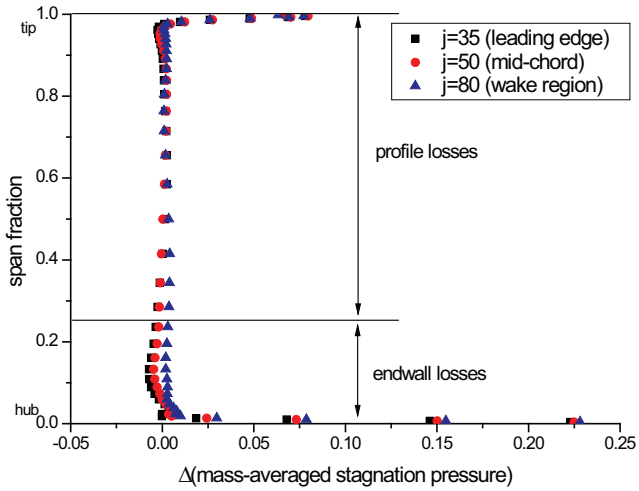


Figure 4 : Mass-averaged pressure losses along the span of the blade

the vertical axis varies from 0 (hub) to 1 (tip). The anticipated variation in the losses as the flow passes around the blade can readily be seen. The stagnation inlet pressure distribution, shown in Fig. 5, should be taken into account to understand this flow behavior. This pressure profile comes from real experimental data, and represents the output from the upstream row. The complex, nonlinear nature of the flow close to the hub and tip regions is demonstrated clearly. It is noticeable from Fig. 3 that the flow solution exhibits unsteady behavior close to the LE and TE regions.

Obviously, the area of greatest interest is the unsteady flow in the wake, and the objective flow metrics are defined for this region. Hence, the position where these metrics are measured in the axial direction is set at $j = 80$, which is well inside the highly viscous wake region. The demarcations of endwall and profile losses are shown in Fig. 4: the former occupies the first 40% of the nodes in the k (radial) dimension starting from the hub ($\sim 25\%$ of span) and the remainder quantifies the profile losses. The definition of these losses is based on the reference value of the inlet stagnation pressure p_0 on each k plane (and not the pressure difference with the inlet r-θ plane), because of the non-uniformity of the boundary condition stagnation pressure profile along the span (Fig. 5).

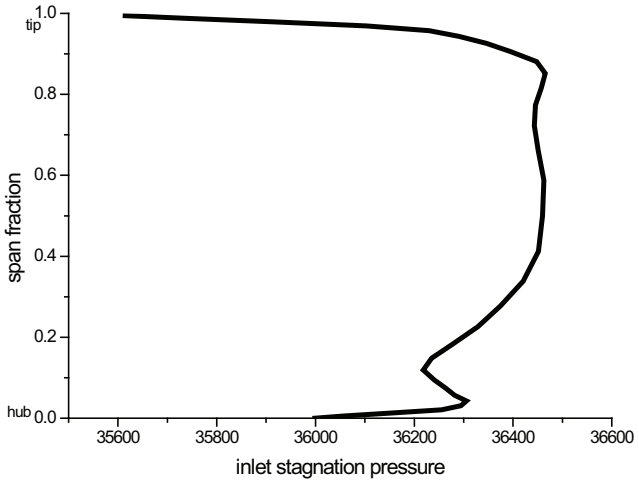


Figure 5 : The inlet stagnation pressure profile

3.3 Objective function formulation

The design optimization of compressor blade geometries has previously been studied by Harvey (2002) from a single-objective perspective. In our multi-objective studies we retain Harvey's objective function, span-averaged blockage for a given mass flow rate, as an essential 1D (throughflow) measure of blade performance, based on the non-uniformity of the flow in the trailing edge plane. This is a normalized function, relative to the specified datum design, including penalty function terms for specific flow characteristic and geometry constraints:

$$f_1 = \frac{B}{B_0} + 250\left(1 - \frac{\dot{m}}{\dot{m}_0}\right)^2 + 0.4max^2\left(0, 1 - \frac{R_{LE}}{R_{LE,0}}\right) + 500max^2\left(0, 1 - \frac{\Delta\theta}{\Delta\theta_0}\right) + 0.5max^2\left(0, 1 - \frac{C}{C_{lim}}\right) \quad (6)$$

In Eq. 6, B represents the blockage, as defined by Eq. 2. This is probably the most important metric in high-speed compressor design. (In highly loaded compressors, the flow tends to separate from the blade under conditions of low mass flow. Flow separation acts as a blockage in the flow path, which limits pressure recovery.) Then, $\dot{m}$ is the mass flow rate; R_{LE} is the minimum radius of the leading edge of the blade; $\Delta\theta$ is the mass-averaged flow turning; C measures the tip clearance of the blade; and C_{lim} is the defined lower limit on tip clearance. The 0 subscripts identify the equivalent quantities for the datum blade geometry, the initial design in the optimization – a real compressor blade design shown in Fig. 2.

The mass flow associated with the design is equality constrained for two reasons. First, if it was not, the inlet dynamic head from the rotor would vary, and this is not modeled by the boundary conditions. Second, if the axial velocity drops, then the inlet static pressure must be higher (since inlet pressure and flow angles are prescribed), so that the static pressure rise across the stator will be lower (outlet pressure is fixed), and the blade row will not be an effective diffuser. Similarly, it is important that, if the mass flow is fixed, the flow turning in the stage should not be reduced during optimization, otherwise the static pressure recovery will not be sufficient. Therefore, control of the flow turning is achieved by treating it as an equality constrained penalty term as well.

In addition, there are two terms in Eq. 6 describing geometrical constraints on the blade. The first limits the sharpness of the blade's leading edge, while the second allows a weighted penalty factor to trade off aerodynamic performance against mechanical proximity. The objective function value is penalized when the blade design has less than C_{lim} (1.5 cm) clearance. Both these penalty terms reflect a concern for robust aerodynamic performance from the design, since these geometric features are closely related to the off-design performance of the blade.

Harvey (2002) found that it was necessary to use a penalty function approach with these constraints in order to successfully navigate the highly constrained, nonlinear search space characteristic of aerodynamic design optimization problems. He established suitable values for the weightings for each of the penalty terms through extensive testing. As discussed in Sect. 3.1, other constraints, such as those on the geometric feasibility of blade designs and on their operational feasibility (a design which produces unsteady flow patterns is not acceptable), are handled as hard constraints – designs violating them are not accepted.

4 Multi-objective Tabu Search optimizer

Our choice of TS as the optimizer is informed by the work of Harvey (2002), who tested a number of metaheuristic methods on a representative single-objective aerodynamic design optimization problem and found TS

to be superior to the GA and SA methods.

Jaeggi, Asselin-Miller, Parks, Kipouros, Bell, and Clarkson (2004) developed the original version of the multi-objective TS (MOTS) variant used here, and executed a performance comparison on a set of unconstrained test functions. Its constraint handling approach and the performance of the algorithm on benchmark constrained optimization problems were presented in Jaeggi, Parks, Kipouros, and Clarkson (2005).

The single-objective TS implementation of Connor and Tilley (1998) is used as a starting point for our multi-objective variants. This uses a Hooke and Jeeves local search algorithm (designed for continuous optimization problems) [Hooke and Jeeves (1961)] coupled with short, medium and long term memories to implement search intensification and diversification as prescribed by Glover and Laguna (1997).

The efficacy of the optimizer on a real multi-objective aerodynamic design problem has been demonstrated by Kipouros, Jaeggi, Dawes, Parks, and Savill (2005b), and details of application-specific enhancements to the optimization algorithm (a different intensification-diversification strategy, a different restart strategy, and an intelligent variable selection scheme based on the idea of *path relinking* [Glover (1999)], which provides enhanced local search capabilities) were presented by Kipouros, Jaeggi, Dawes, Parks, and Savill (2005a).

5 Applications and analyses

The first study presented in this paper investigates the trade-off between the endwall and profile losses for a constrained level of blockage, and illustrates how a designer can distribute the secondary losses along the span and control the secondary flow effects on a compressor blade. Then the results from a three-objective optimization, considering the simultaneous minimization of profile losses, endwall losses, and blockage are presented, demonstrating the ability of the optimizer to navigate effectively in the search space of high dimensionality aerodynamic design problems.

Both test cases use the objective function formulation given in Sect. 3.3 subject to the same set of penalty function constraints, and the objective flow metrics are those defined in Sect. 3.2. In addition, the inlet boundary conditions presented in Fig. 5 are maintained throughout, and each optimization run was initiated from the datum geometry shown in Fig. 2. The flow metrics associated with this geometry are presented in Tab. 1.

Table 1 : Flow metrics for the datum design

Flow metric	Value
$\dot{m}$: Annulus mass flow (kg/s)	15.7142
$\dot{S}$: Entropy generation (J/K)	1.36376
N: Blade loading (N)	442.872
p_{in}: Mass-averaged inlet static pressure (Pa)	34318
p_{out}: Mass-averaged outlet static pressure (Pa)	35322.7
P_{in}: Mass-averaged inlet stagnation pressure (Pa)	36448.3
P_{out}: Mass-averaged outlet stagnation pressure (Pa)	36294.7
$\Delta\theta$: Mass-averaged flow turning (deg)	22.2076
$V_{s.d.}$: Mass-averaged velocity standard deviation (-)	8.89887
B: Blockage (-)	0.191383
Φ: Loss coefficient (%)	7.210
$\phi_{profile}$: Mass-averaged profile losses (-)	0.339676
$\phi_{endwall}$: Mass-averaged endwall losses (-)	0.547357

In all optimization runs the TS optimizer used the following parameter settings. The number of tabu points (the size of the short-term memory) was 15. After 25 successive iterations without refining the Pareto front, the search was intensified in the region of previously-found Pareto-optimal solutions, stored in the intensification memory. After 75 iterations without Pareto front refinement, the search was diversified to a previously unexplored region of the search space. After 95 iterations without Pareto front refinement, the search step sizes were reduced and the search re-started from a point on the current Pareto front. Every 20 optimization steps the intelligent variable selection scheme was refreshed. The alternative restart strategy was executed after 5 step size reductions. If the intensification memory contained more than 10 solutions an intensification step was executed instead of diversification. See Kipouros, Jaeggi, Dawes, Parks, and Savill (2005a) for details of these optimizer features.

5.1 Test case 1 – profile losses vs endwall losses

In this case study we seek to increase the uniformity of the secondary flows for the compressor blade shown in Fig. 2 by balancing the profile and endwall losses for the same level of blockage in the wake region. Blockage is therefore treated as an additional equality constraint, and the objective function formulation of Eq. 6 modified to:

$$f_{losses} = \frac{\phi}{\phi_0} + 2.5\left(1 - \frac{B}{B_0}\right)^2 + 250\left(1 - \frac{\dot{m}}{\dot{m}_0}\right)^2 \quad (7)$$
$$+ 0.4max^2\left(0, 1 - \frac{R_{LE}}{R_{LE,0}}\right) + 500max^2\left(0, 1 - \frac{\Delta\theta}{\Delta\theta_0}\right)$$
$$+ 0.5max^2\left(0, 1 - \frac{C}{C_{lim}}\right)$$

The weighting for the blockage penalty term was set after testing the effect of various choices on search performance.

In Eq. 7, ϕ is the statistical meassure of mass-averaged stagnation pressure difference (as defined in Eq. 4) between a specific fraction of the span of the blade, in the wake region, and the corresponding position of the flow at the inlet of the passage. Hence:

$$\phi = \sum_{i=1}^{km} \Delta\overline{p_{stag}}_i \quad (8)$$

where *km* is the number of grid nodes in the radial direction. In this case, there are 45 nodes in the *k*-direction of the structured mesh, of which, 19 are used to calculate the endwall losses ($\sim$25% of span), and the remaining 26 to calculate the profile losses.

In this case study, additional aerodynamic constraints were used in evaluating candidate designs. Many designs exhibit unsteady behavior as characterized by negative values of the mass-averaged pressure difference $\Delta\overline{p_{stag}}$. If a negative value of $\Delta\overline{p_{stag}}$ is observed at the mid-span position of the blade, the design is deemed to be aerodynamically infeasible. If negative values are observed in too many (more than 15%) of the other grid nodes, then the design is also deemed to be aerodynamically infeasible. If fewer than 15% of the $\Delta\overline{p_{stag}}$ values are negative, then the design is deemed to be aerodynamically feasible, but, as negative values of $\Delta\overline{p_{stag}}$ are unphysical, such values are replaced by the value at mid-span before the flow metrics are evaluated.

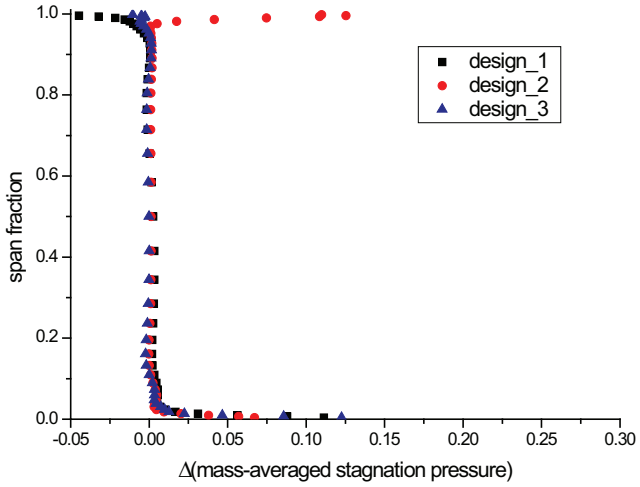


Figure 6 : Classification of aerodynamic infeasible designs in terms of secondary losses

Fig. 6 illustrates the different cases of aerodynamic infeasibility in terms of secondary losses. Design 1 has more than the acceptable number of negative values for $\Delta\overline{p_{stag}}$ and, as a consequence, is deemed aerodynamically infeasible. Design 2 has some, but not too many, negative values of $\Delta\overline{p_{stag}}$, so it is feasible, and would be evaluated after the negative values have been corrected, as described above. Design 3 is aerodynamically infeasible because $\Delta\overline{p_{stag}}$ is negative at mid-span.

On average, 20 CFD evaluations were executed per optimization iteration. Only 4,300 designs were found to be feasible out of the 36,000 candidate designs visited in the search space of this problem. The pattern of the search in objective space is shown in Fig. 7. This optimization run took 15 weeks on a 5-node cluster of AMD Opteron 64-bit 2.4 GHz processors.

Many discontinuities in the design space of this heavily constrained optimization problem were revealed, as shown in Fig. 7, and the Pareto-optimal set found occupies only a very small region, which was extensively explored by the optimizer. The large gap in the search pattern is due to geometrically and aerodynamically infeasible regions of the design space (creating a discontinuity in the objective landscape). The close-up view of the Pareto front found, shown in Fig. 8, reveals that the area of global optimality is separated from a sub-optimal

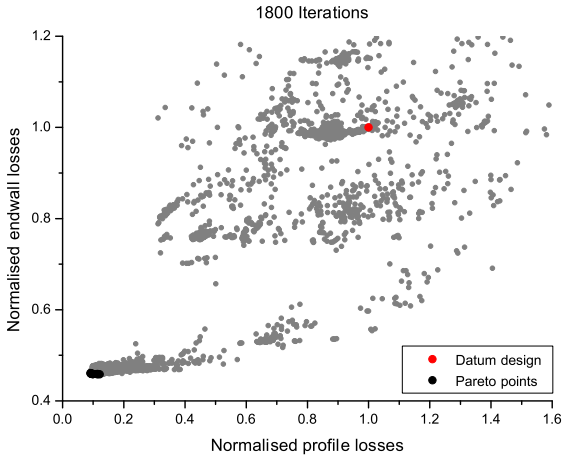


Figure 7 : The optimization search pattern and the Pareto front found for test case 1

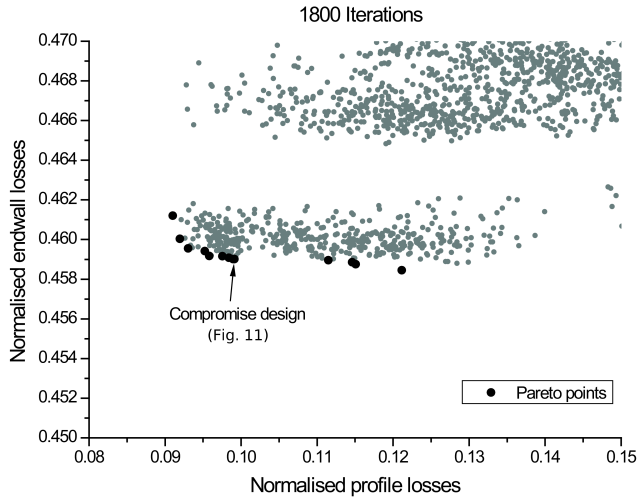


Figure 8 : A close-up of the optimization search pattern and the Pareto front found for test case 1

valley by another discontinuity in objective space. Nevertheless, the MOTS optimizer managed to navigate the search space successfully despite these difficult features.

Tab. 2 presents the flow metrics for the lowest profile losses design (Fig. 9), the lowest endwall losses design (Fig. 10) and a compromise (Fig. 11) optimal design. There is only 0.1% variation in mass flow rate and an average reduction of 2% (relative to the datum design) in blockage for all these optimal designs.

Table 2 : Optimized flow metrics for test case 1

Flow metric	Lowest profile losses optimum	Compromise design	Lowest endwall losses optimum
$\dot{m}$	15.7306	15.7329	15.7396
$\dot{S}$	0.802852	0.823558	0.854934
N	488.298	488.424	489.353
p_{in}	34306.6	34306.0	34303.9
p_{out}	35317.8	35317.6	35317.7
P_{in}	36408.9	36409.4	36408.9
P_{out}	36280.7	36280.6	36281.1
$\Delta\theta$	22.9595	22.9657	22.9875
$V_{s.d.}$	8.94788	8.94832	8.9565
B	0.187827	0.187221	0.187839
Φ	6.098	6.123	6.071
$\phi_{profile}$	0.032035	0.0352825	0.0366724
$\phi_{endwall}$	0.247973	0.247566	0.247902
$F_{profile}$	0.0910047	0.0989504	0.121112
$F_{endwall}$	0.46121	0.459021	0.458456

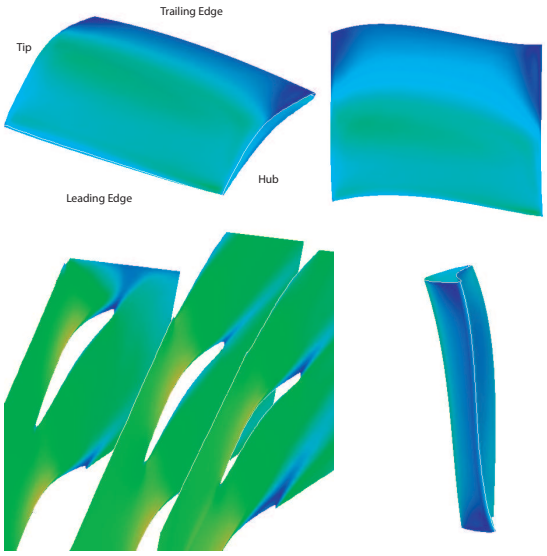


Figure 9 : The optimized geometry for lowest profile losses (Fig. 8) – as Fig. 2

Interestingly, for all these optimal designs there is a 2% increase in the static pressure rise as a fraction of inlet

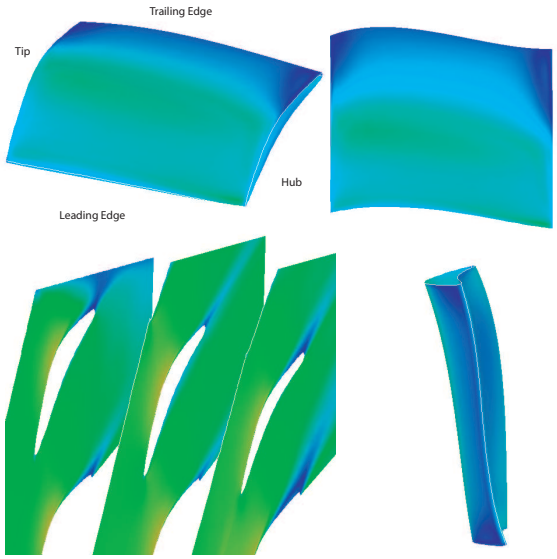


Figure 10 : The optimized geometry for lowest endwall losses (Fig. 8) – as Fig. 2

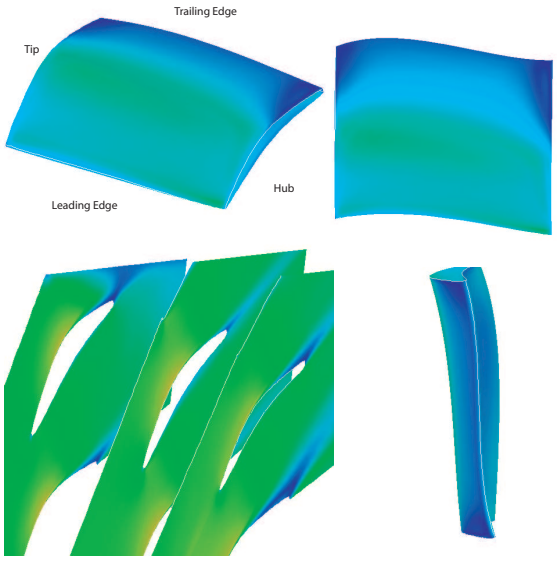


Figure 11 : The optimized geometry for a compromise design (Fig. 8) – as Fig. 2

dynamic head, relative to the datum blade performance. The corresponding values of this metric are 0.481 for the optimal designs and 0.471 for the datum. Significant improvement in the loss coefficient Φ, as defined in Eq. 5, is revealed in Tab. 2. The datum value is 7.21% and this is reduced by 15% or more for all three optimal designs. In addition, entropy generation rate $\dot{S}$ has been reduced substantially (by 40% on average) confirming its correlation with secondary losses. Finally, mass-averaged velocity standard deviation $V_{s.d.}$ is important in the context of the constraint on blockage, and a slightly increased value of this metric is maintained throughout the optimal designs.

A few general geometrical characteristics distinguish the optimal designs from the datum blade shape. Geometries which exhibit much thicker 2D blade profiles, with the suction side camber distribution peaking just before the mid-chord point, can dramatically decrease secondary losses in the wake region of compressor blades (normalised profile losses by 91% and normalised endwall losses by 54%). Despite the small variation in the optimal blade shapes, there are some detailed refinements in the 3D blade surfaces, responsible for the differences in performance between them. Fig. 9 and Fig. 10 highlight the key characteristic: the hub-mid-span section of the lowest endwall losses design is shifted against the flow direction by a small fraction of the chord. In addition, blade thickness is increased in the radial direction for all the optimal designs.

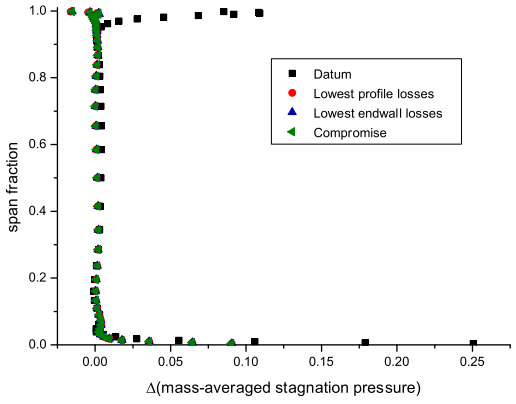


Figure 12 : The distribution of profile losses along the span of the optimal designs for test case 1

Fig. 12 shows the distributions of secondary losses along the span of the datum blade and the three selected optimal designs. All the optimal designs give a very similar loss distribution, and only in the tip region close to the wall

is the flow predicted to be unsteady. Small differences in the losses in the mid-span area of the optimal blades distinguish their performance. The flow patterns around these blades exhibit smooth changes in velocity distribution throughout the passage, and, more importantly, the profile of bad flow features is spread evenly along their trailing edge regions.

Fig. 13 presents the velocity contours for the selected compromise optimal design from test case 1 in comparison with the datum design. The improvement in the distribution of poorer flow quality features across the blade is clear. The area with separated flow is eliminated towards the rear end of the suction surface, especially at the TE-tip corner, and also from the mid-span area.

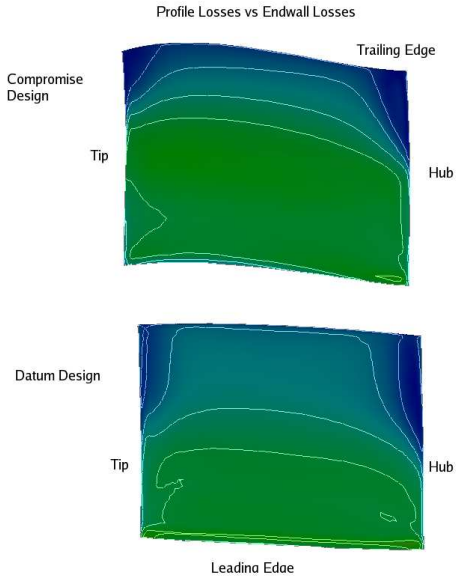


Figure 13 : The velocity contours for the test case 1 compromise design and the datum design

The rate of optimization progress on this test case is shown in Fig. 14. The general area of optimality is located approximately in the first 400 optimization iterations after the execution of three step size reductions. At this stage there are two designs on the known Pareto front (Fig. 15). Fig. 16 reveals that the other MOTS feature particularly assisting the search in the early stages was the intelligent variable selection scheme, which was refreshed every 20 iterations. With appropriate design parameter step sizes, the optimizer proved able to explore this region of search space efficiently, and, after another reduction in the step sizes, the area was refined further and a rich Pareto front was revealed at that stage of the optimization process.

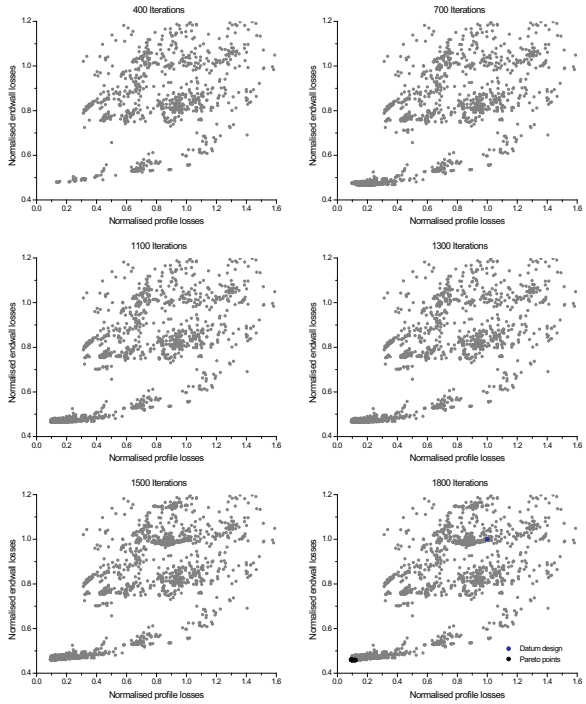


Figure 14 : Snapshots of the optimization search pattern for test case 1

At the 800th optimization step the restart strategy was executed, and, following a refinement in the step sizes, the optimizer was able to advance the Pareto front (Fig. 14 and Fig. 15). The restart strategy, in which the search was restarted from an extreme Pareto point, reinvigorated the search and assisted in refining the optimal region.

After locating a new optimal area of design space, the optimizer has to reduce the step sizes in order to refine the search in this region. It is apparent in Fig. 15 that five Pareto designs could be found in consecutive successful steps on the first visit of the optimizer to this area of search space (at 1300 iterations in Fig. 16). Finally, after four step size reductions executions, the region of global optimality was explored and refined in detail, and 13 optimal designs comprise the final Pareto front shown in Fig. 8.

The relatively short Pareto front found for this test case is noteworthy. This is perhaps to be expected since the overall secondary losses are significantly reduced, compared with those associated with the datum geometry,

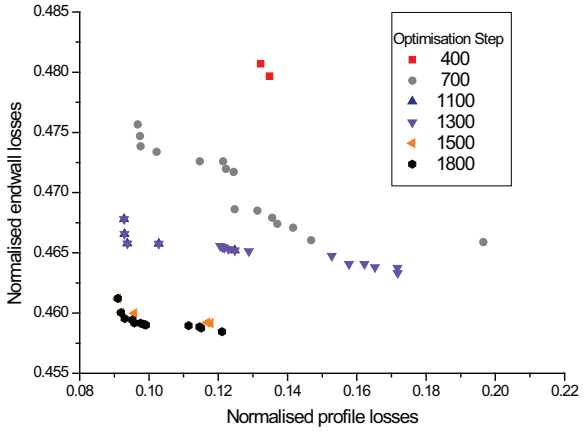


Figure 15 : The development of the Pareto front in test case 1

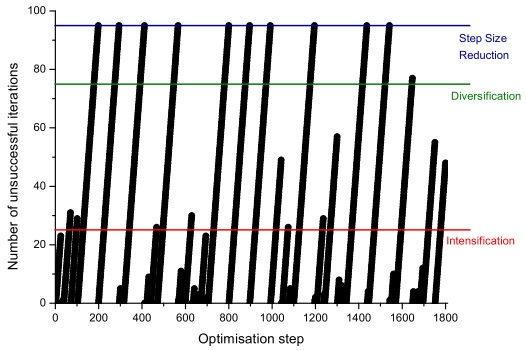


Figure 16 : The optimization search pattern in test case 1, shown through the number of consecutive unsuccessful iterations

and, in consequence, the available trade-off between profile and endwall losses is somewhat restricted.

5.2 Test case 2 – profile vs endwall losses vs blockage

To test the capabilities of the system on problems with more than two objectives, a three-objective problem was formulated. A combination of the same flow metrics formed an optimization problem with three figures of merit, subject to the same aerodynamic and geometric constraints as in Eq. 6. Test case 1 was modified, with blockage now treated as an objective, rather than a constraint. The potential size of the Pareto front is substantially increased as the number of objectives rises. This means that significantly more computational time is needed to locate this front.

The Pareto trade-off surface between profile losses, endwall losses and blockage, shown in Fig. 17, was revealed after 52,800 CFD evaluations, with on average 22 per optimization step. The 2,400 iterations were executed in 23 weeks on the same 5-node cluster as used for test case 1.

54 optimal designs define the Pareto surface, which is rotated about the blockage axis to give the different views presented in Fig. 17. The black dots are points in 3D space, while the red, green and blue dots present the projections on the endwall losses vs profile losses, endwall losses vs blockage, and profile losses vs blockage planes. Only 6,322 feasible designs were found. The optimization search pattern revealed is shown in Fig. 18.

The discontinuous Pareto surface contains two clusters in diametrically opposite regions of the 3D design space, and the third view in Fig. 17 highlights the gap between them. The region of the search space in which the designs perform better in terms of endwall losses is underexplored, which indicates that more optimization steps are needed for a thorough search of the design space. However, six Pareto designs lie in this area, and the trend of the trade-off surface between profile losses and blockage is outlined (blue points in the top-right corner in Fig. 17).

Fig. 19, Fig. 20 and Fig. 21 illustrate the optimal designs for minimum profile losses, endwall losses and blockage, respectively. Tab. 3 presents their flow metrics, and reveals that all of the optimal designs have reduced values for all of the objectives relative to the datum design. Even though less than a 0.5% reduction in mass flow rate (relative to datum) has been recorded, only the geometry for lowest profile losses exhibits an improvement (of 0.2%) in the static pressure rise through the passage (the value of this metric for the optimal design is 0.472, while for the datum design it is 0.471). In contrast, the blade shapes for lowest endwall losses and blockage cause a 0.4% and a 0.6% reduction in the static pressure rise as a fraction of inlet dynamic head, respectively. However, the loss coefficient has been improved for the designs with lowest profile losses and blockage by 9.8% and 3.5%, respectively, but not for the lowest endwall losses design, which shows a 4% increase in this performance measure. The entropy generation rate is reduced significantly for all of these extreme optimal designs (by more than 40%).

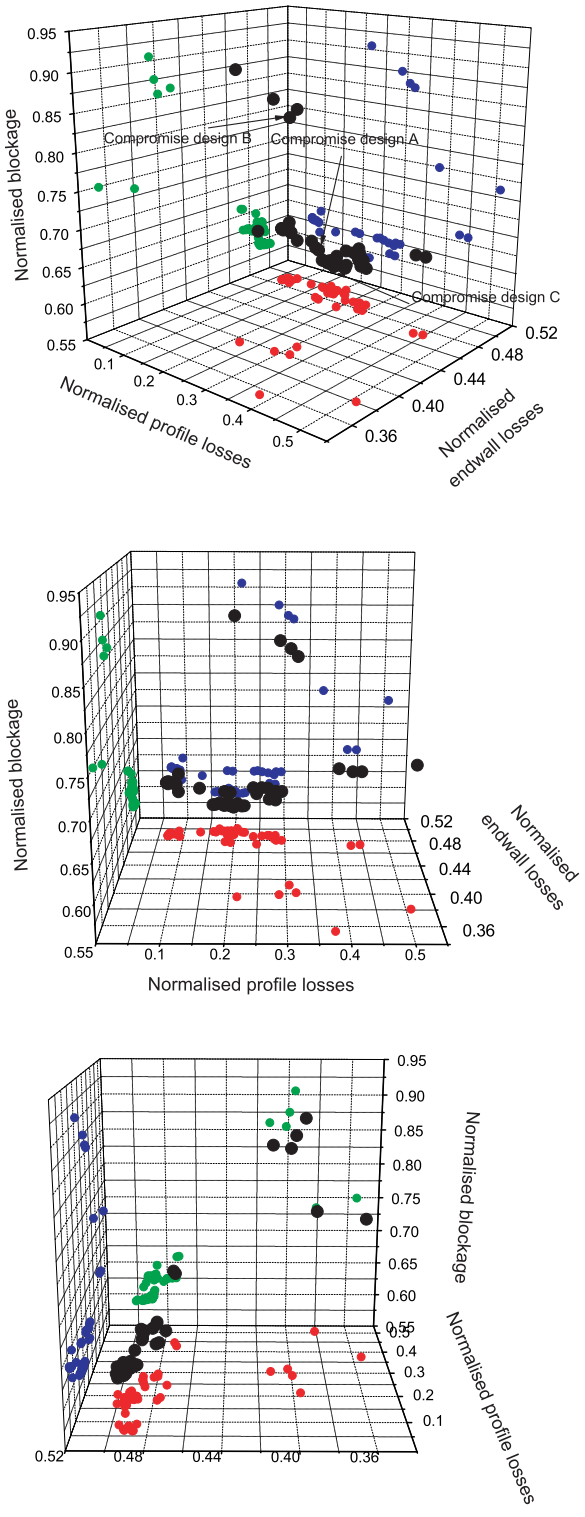


Figure 17 : The Pareto front found in test case 2 from three viewing angles

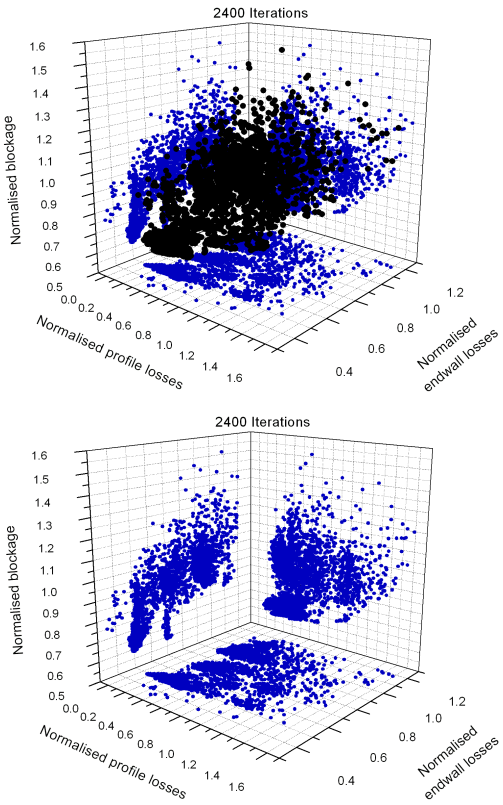


Figure 18 : The optimization search pattern, in 3D and 2D projections, for test case 2

Tab. 4 presents the extreme values that each objective function takes as the Pareto front develops, and, in conjunction with Tab. 3, reveals that there is a strong trade-off between endwall losses and the other two objectives (designs giving low endwall losses have comparatively high values for profile losses and blockage, and vice versa), whereas the trade-off between profile losses and blockage is less pronounced.

Analysis of the performance of some of the compromise designs (Fig. 22, Fig. 23 and Fig. 24) lying on the Pareto surface shown in Fig. 17 support these observerations. Tab. 5 presents their flow metrics.

A maximum of 1% variation in mass flow is recorded. Entropy generation rate is reduced for all these designs, along with improvements in the objective flow metrics, but compromise design B presents an undesirable combination of these metrics. A first indication of this is an increase in mass-averaged velocity standard deviation for a lower value of blockage. In consequence, the loss coef-

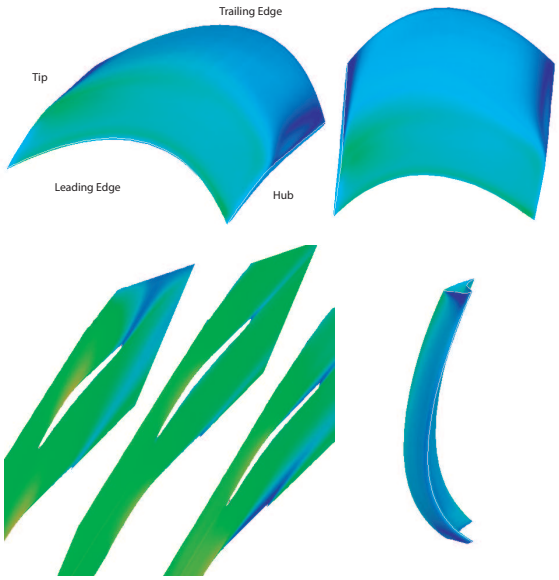


Figure 19 : The optimized geometry for lowest profile losses (Fig. 17) – as Fig. 2

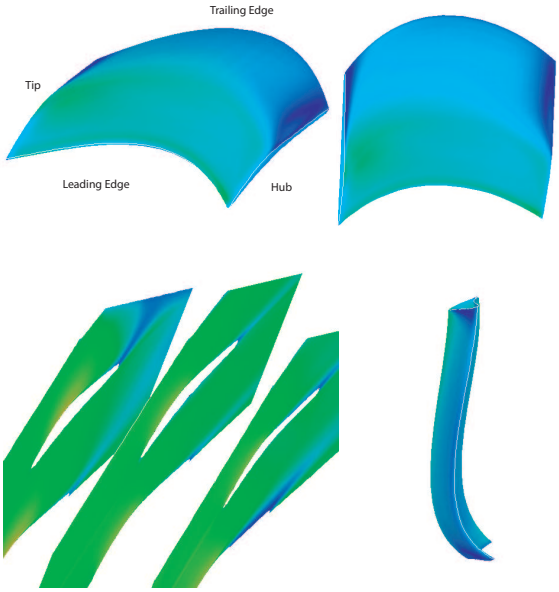


Figure 21 : The optimized geometry for lowest blockage (Fig. 17) – as Fig. 2

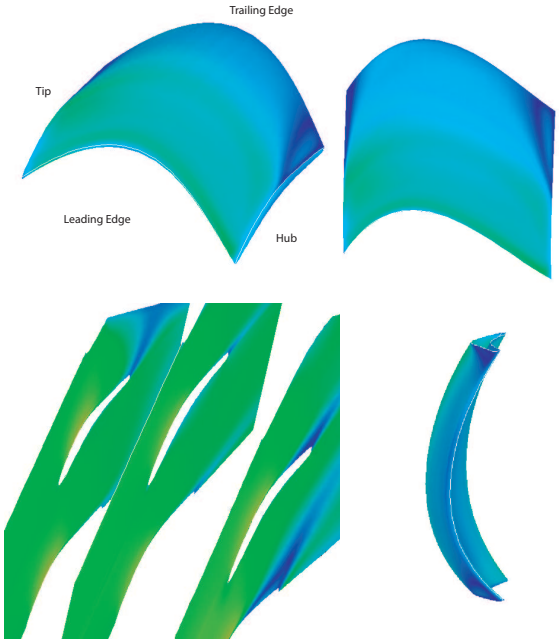


Figure 20 : The optimized geometry for lowest endwall losses (Fig. 17) – as Fig. 2

Table 3 : Extreme optimized flow metrics for test case 2

Flow metric	Lowest profile losses optimum	Lowest endwall losses optimum	Lowest blockage optimum
$\dot{m}$	15.6825	15.6821	15.6402
$\dot{S}$	0.843567	0.791276	0.767695
N	429.160	461.878	425.331
p_{in}	34323.1	34322.2	34335.5
p_{out}	35310.5	35306.2	35311.3
P_{in}	36412.5	36417.6	36419.0
P_{out}	36278.2	36260.5	36275.4
$\Delta\theta$	22.5674	23.7639	22.2639
$V_{s.d.}$	8.63363	9.39396	8.3880
B	0.120286	0.142147	0.111664
Φ	6.427	7.497	6.959
$\phi_{profile}$	0.028359	0.190513	0.065286
$\phi_{endwall}$	0.263806	0.126721	0.268739
$F_{profile}$	0.068580	0.377604	0.205007
$F_{endwall}$	0.487585	0.354391	0.501052
$F_{blockage}$	0.631419	0.749385	0.588706

ficient is increased by 10% for this design, while compromise designs A and C improve this performance metric

Table 4 : Extreme objective values at various stages in test case 2

Number of iterations	$F_{profile}$	$F_{endwall}$	$F_{blockage}$
540	0.1699	0.499473	0.769866
	1.05236	0.994402	1.00782
1000	0.123485	0.354391	0.691253
	0.509026	0.994402	0.942785
1200	0.123485	0.354391	0.691253
	0.509026	0.994402	0.942785
1540	0.123485	0.354391	0.63559
	0.509026	0.521492	0.942785
2000	0.101713	0.354391	0.593134
	0.509026	0.520485	0.905662
2400	0.068580	0.354391	0.588706
	0.509026	0.501052	0.905662

by 8.9% and by 5.6%, respectively. However, the static pressure rise as a fraction of inlet dynamic head is only increased for compromise design A (by 1%).

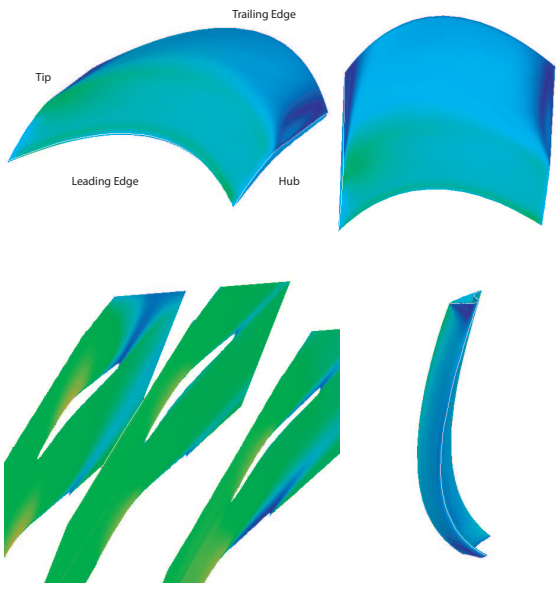


Figure 22 : The optimized geometry for compromise design A (Fig. 17) – as Fig. 2

The geometrical characteristics of the optimal design for lowest blockage, shown in Fig. 21, are very similar to

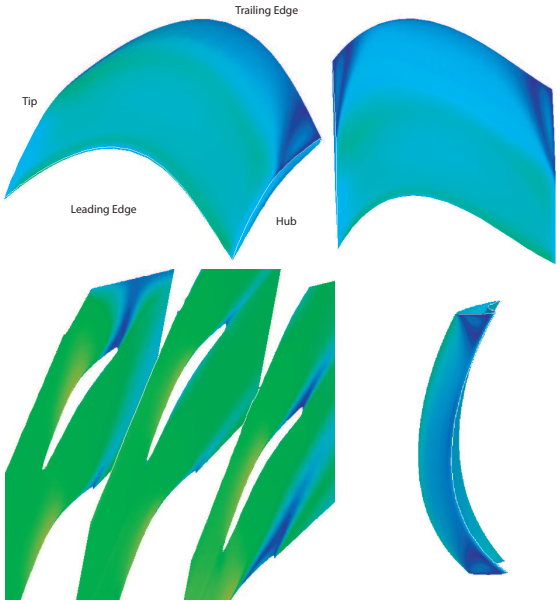


Figure 23 : The optimized geometry for compromise design B (Fig. 17) – as Fig. 2

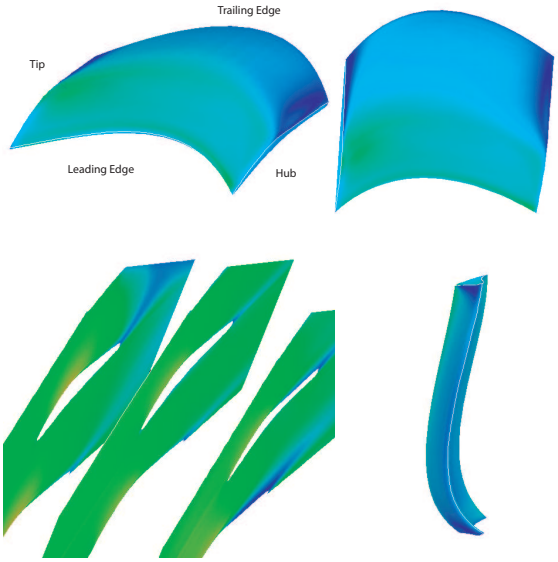


Figure 24 : The optimized geometry for compromise design C (Fig. 17) – as Fig. 2

those found in previous studies in which blockage was minimized (Kipouros, Jaeggi, Dawes, Parks, Savill, and Clarkson (2008)). The downstream sweep of the mid-

Table 5 : Flow metrics for selected compromise designs for test case 2

Flow metric	Design A	Design B	Design C
$\dot{m}$	15.7476	15.5536	15.6636
$\dot{S}$	0.70788	0.73071	0.881915
N	430.223	446.857	429.087
p_{in}	34304.9	34359.3	34329
p_{out}	35309.8	35303.4	35310.7
P_{in}	36414.6	36419.7	36417.6
P_{out}	36276.1	36256.1	36275.5
$\Delta\theta$	23.0292	23.4832	22.4128
$V_{s.d.}$	8.76655	9.82165	8.44371
B	0.119129	0.158312	0.112325
Φ	6.565	7.940	6.803
$\phi_{profile}$	0.063598	0.087578	0.059164
$\phi_{endwall}$	0.257864	0.203924	0.26807
$F_{profile}$	0.19415	0.305924	0.174042
$F_{endwall}$	0.476463	0.412085	0.496716
$F_{blockage}$	0.624803	0.859948	0.5913

span area is a common characteristic of these blades, and, indeed, of all the designs exhibiting low blockage values on the Pareto front for this test case.

In consequence, other three-dimensional facets, in the radial and circumferential directions, combined with backwards sweep of the mid-span area can then improve secondary losses. Fig. 19 to Fig. 24 present a normal view of the suction side and a downstream side view of the optimal designs analyzed in this section. It is clear that a spanwise camber distribution, with its peak advancing deeper in the radial direction, is responsible for lower secondary losses.

The lowest blockage design exhibits this characteristic close to the hub region, and then follows the design for lowest profile losses, and at the same time both the hub and tip sections are slightly leaned. Fig. 20 demonstrates that not only is the TE camber moving towards the tip, in order to achieve a significant reduction in endwall losses, but likewise the position of negative sweep in the mid-span area of the blade. The complexity of this geometry increases as the hub and tip sections are leaned more, while the top view reveals similarities with the optimal design for lowest endwall losses (Fig. 10), when blockage is constrained around its datum value, in the LE-hub region.

The same geometrical characteristics are exhibited by the compromise designs (Fig. 22, Fig. 23 and Fig. 24) as the balance between the objectives changes. Hence, compromise design A is similar to the lowest profile losses optimum, compromise design B to the lowest endwall losses optimum, and compromise design C to the lowest blockage optimum. The most desirable blend of these geometrical features is not clear, but a combination with the dominant characteristic for lowest profile losses looks promising.

The velocity distributions around the optimal blades are smooth and uniform in their viscous wake region. Fig. 25 and Fig. 26 illustrate the secondary losses distributions along the span of the blade surfaces compared with that for the datum design. The fact that all these Pareto-optimal designs reduce the production of secondary losses is clearly demonstrated, and a trade-off between profile and endwall losses has been developed.

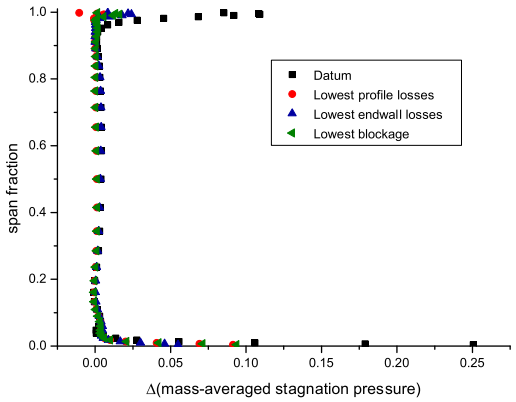


Figure 25 : The distribution of profile losses along the span of the extreme optimal designs for test case 2

However, the flow separates and reattaches in the TE-hub region of the lowest endwall losses blade (Fig. 20), and this may contribute to the poor aerodynamic performance of this blade relative to the others. In addition, as already mentioned, the design area associated with lowest endwall losses is under-explored, and only sub-optimal designs may therefore have been found in this area.

Fig. 27 presents the velocity contours for various optimal geometries from test case 2. All the designs have low values for the blockage objective apart from the lowest end-

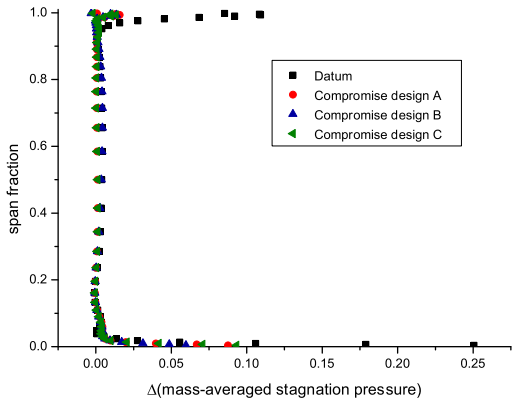


Figure 26 : The distribution of profile losses along the span of the compromise optimal designs for test case 2

wall losses blade. This shows a step increase in blockage clearly associated with development of 3D vorticity, but concentrated only in a small area on the TE-hub corner and in a similarly small area of the TE-tip corner.

The optimal geometry for lowest endwall losses also has the highest value of the profile losses flow metric. Hence, the area of separated flow is larger compared with the other optimal geometries. The strength of the 3D vortex varies throughout the trade-off surface according to the value of blockage. Unsurprisingly the low endwall losses/high blockage blade exhibits a markedly different geometry to the other compromise optima.

Initially, the search of the 3D design space is managed well by the MOTS optimizer, thanks to the effectiveness of its intensification strategy and intelligent parameter selection technique, and good progress is made in advancing all three objectives. 45 designs form the Pareto front shown in Fig. 28 after 540 optimization steps, and the high complexity of the trade-off between these objectives is highlighted by the representation of the 3D Pareto front in parallel coordinates [Inselberg (1985)] shown in Fig. 28 and Fig. 29. In this representation the objective functions are indexed on the horizontal axis and the objective values (normalized to their minimum-maximum range, as in Tab. 4) are plotted vertically, with the values associated with each design being joined by a line.

Fig. 28 and Fig. 29 show the progress in advancing the Pareto front. After 540 iterations, the area associated with low endwall losses is further explored, and the

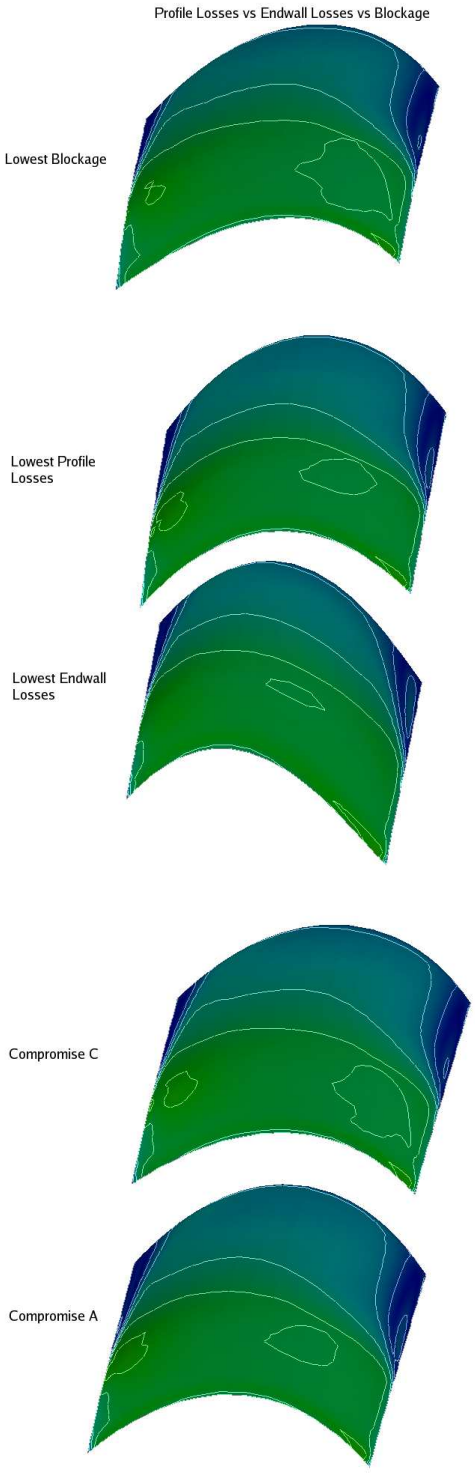


Figure 27 : The velocity contours for various optimal designs the test case 2

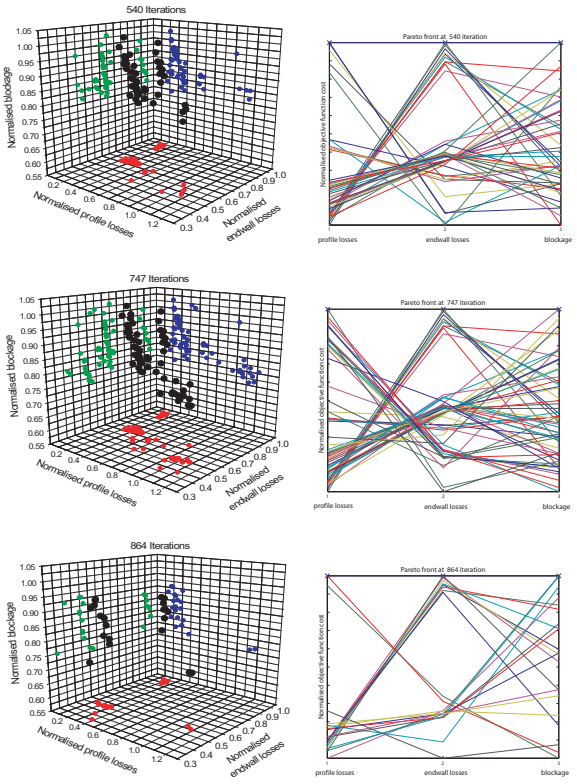


Figure 28 : The Pareto front for test case 2, at 540, 747 and 864 iterations, with the corresponding parallel coordinates representation

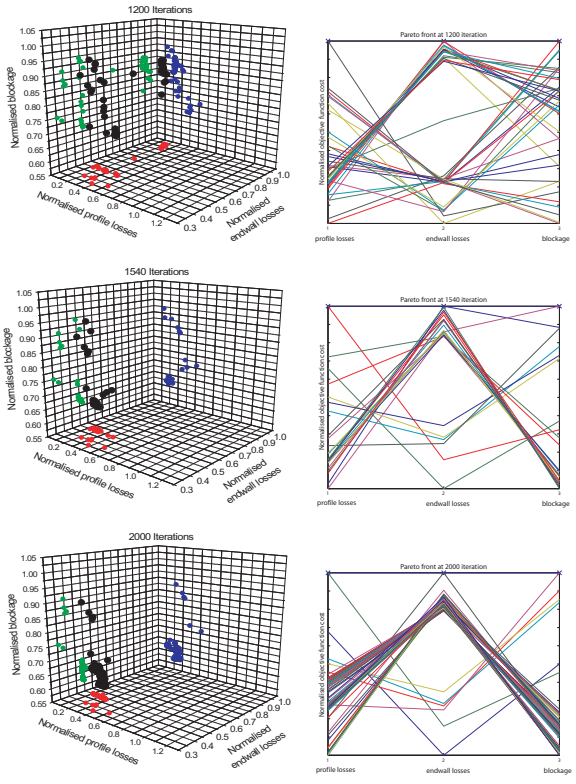


Figure 29 : The Pareto front for test case 2, at 1200, 1540 and 2000 iterations, with the corresponding parallel coordinates representation

Pareto surface is enriched with 15 more designs after 747 iterations, mainly with increased profile losses. Then, this area is refined, while blockage reached the lowest possible value that could be achieved with the initial step size. Secondary losses gradually reduced until the optimizer found the design area with lowest profile losses (at the 864th iteration), indicated by its maximum value in Tab. 4 at 1000 iterations. At this stage, the Pareto front consists of 21 designs.

Fig. 30 clearly demonstrates that the most important MOTS features in this stage of the search were intensification, the parameter selection technique and the intensification/diversification strategy. Continuous progress is exhibited in Fig. 30 after many intensification steps. In some cases, where intensification did not promote progress, the parameter selection techique assisted the optimizer, and further progress was then made. Eight times the threshold for diversification was exceeded. In all cases the size of the intensification memory exceeded the threshold value, and therefore an intensification step was executed instead of a diversification one. Five of these eight intensifications resulted in the optimization then making further progress.

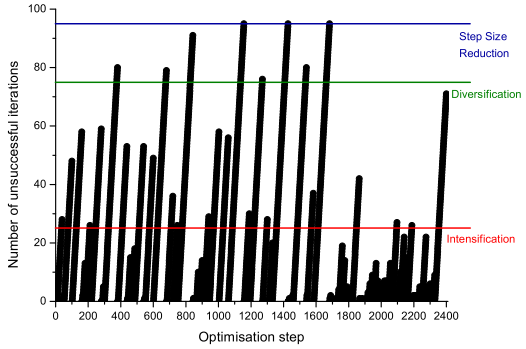


Figure 30 : The optimization search pattern for test case 2, shown through the number of consecutive unsuccessful iterations

When step size reduction was executed for the first time, the design area with good blockage characteristics could be explored better (Fig. 28 and Fig. 29). The variation in blockage mainly produced compromise designs in the profile losses vs endwall losses trade-off. The execution of step size reduction for the second time improved the search in low blockage area, while at the same time further progress in reducing the level of endwall losses is revealed (at the 1540th iteration, Fig. 29).

Fig. 29 illustrates the progress in the Pareto front after three step size reductions, and significant progress in the lowest blockage area is observed (at the 2000th iteration). Not only is blockage improved, but also many designs exhibit lower profile losses, and the number of designs lying on the Pareto front reaches its highest value of 71. Further reductions in blockage together with profile losses is recorded in Tab. 4 and the final trade-off surface is pictured in Fig. 17.

The continuous progress made by the optimizer in the 3D design space shown in Fig. 30 illustrates that the set of MOTS control parameters used is suitable for problems with more than two objectives. It is anticipated that, given more iterations, the area featuring lower endwall losses designs would be further explored, and, in consequence, the region of global optimality for this test case will be found. The optimizer navigates more efficiently in the lowest endwall losses design space with large step sizes. Hence, execution of the restart strategy is expected to be beneficial. A more detailed presentation and discussion of these results can be found in Kipouros (2006).

6 Conclusions

The results for the foregoing studies demonstrate that our multi-objective integrated turbomachinery design optimization system, MOBOS3D, can successfully tackle realistic real-world problems, negotiating the highly constrained, nonlinear search space, and presenting the designer with a range of designs showing the trade-offs between the objectives under consideration, giving insight into the nature of the design space and suggesting innovative designs for further consideration. The importance and the value of optimization in real-world aerodynamic design is proved and validated.

The factors influencing the efficiency of turbomachinery blades and the trade-offs between them are extremely complex. Therefore this topic was investigated further. New objective functions were defined and carefully modelled to evaluate individually the profile losses and endwall losses, in order to improve understanding of the trade-offs between them in design. These investigations required the tackling of a three-objective problem, and the effectiveness of our MOTS variant on this higher dimension problem was demonstrated successfully.

Furthermore, a methodology has been introduced for the analysis of multi-objective optimization results which enables the designer to understand the behavior of the particular optimization technique in the context of the nature of the engineering discipline under investigation. Thus, optimization modeling may be viewed as an essential procedure for the successful exploration of real-world engineering design problems and identification of innovative new solutions.

Through true multi-objective engineering design optimization additional techniques and tools can be exploited to provide a better understanding of the design process and facilitate its improvement. Post-optimization analysis is an important stage of the process in which the objective functions are related to the design parameters, enabling physics-based optimization to be performed Lian and Liou (2005); Kipouros, Mleczko, and Savill (2008). When these techniques are deployed proactively during the design process then significant improvements in the performance of the computational design system can be achieved, as demonstrated by Kipouros, Ghisu, Parks, and Savill (2008).

The aerodynamic analyses of the optimal designs found for each case study proved that the compromise blade shapes exhibit robust behavior for many crucial, for the efficiency of the machine, flow characteristics. As expected, the behavior of the entropy generation rate metric is nonlinear through the optimal designs of these test cases. Only when blockage is constrained does the minimization of profile losses reduce the entropy generation rate monotonically. A four-objective optimization, considering all the flow metrics described in Sect. 3.2 and entropy generation rate, might reveal more robust designs, chosen from the compromise region of the trade-off surface.

In addition, these studies demonstrated that local search is vital in aerodynamic design optimization problems. Even though a few designs might represent an optimal design area, only detailed exploration can manage the appropriate refinements in the optimal blade shapes, in

order to achieve a generic performance improvement.

Acknowledgement: The first author gratefully acknowledges the support of the Embiricos Foundation and the Cambridge European Trust. The second author acknowledges the support of the UK Engineering and Physical Sciences Research Council (EPSRC) under grants numbers GR/R64100/01 and EP/E001777/1.

References

Aarts, E.; Korst, J. (1989): *Simulated Annealing and Boltzmann Machines: A Stochastic Approach to Combinatorial Optimisation and Neural Computing*. John Wiley & Sons.

ACARE (2002): *Strategic Research Agenda 1*. Advisory Council for Aeronautics Research in Europe.

ACARE (2004): *Strategic Research Agenda 2*. Advisory Council for Aeronautics Research in Europe.

Alexandrov, N. (2005): Editorial – multidisciplinary design optimization. *Optimization and Engineering*, vol. 6, no. 1, pp. 5–7.

Aly, S.; Ogot, M.; Pelz, R. (1996): Stochastic approach to optimal aerodynamic shape design. *Journal of Aircraft*, vol. 33, no. 5, pp. 956–961.

Amirante, R.; Catalano, L. A.; Dadone, A.; Daloiso, V. S. E. (2007): Design optimization of the intake of a small-scale turbojet engine. *CMES: Computer Modeling in Engineering & Sciences*, vol. 18, no. 1, pp. 17–30.

Bloor, M. I. G.; Wilson, M. J. (1995): Efficient parametrization of generic aircraft geometry. *Journal of Aircraft*, vol. 32, no. 6, pp. 1269–1275.

Chiba, K.; Obayashi, S.; Nakahashi, K.; Morino, H. (2005): High-fidelity multidisciplinary design optimization of wing shape for regional jet aircraft. *Lecture Notes in Computer Science, Springer-Verlag*, vol. 3410, pp. 621–635.

Connor, A.; Tilley, D. (1998): A Tabu Search method for the optimisation of fluid power circuits. *Journal of Systems and Control*, vol. 212, pp. 373–381.

Dawes, W. N. (1988): Development of a 3D Navier-Stokes solver for application to all types of turbomachinery. ASME 88-GT-70.

Dawes, W. N.; Kellar, W. P.; Harvey, S. A.; Dhanasekaran, P. C.; Savill, A. M.; Cant, R. S. (2003): Managing the geometry is limiting the ability of CFD to manage the flow. AIAA-2003-3732.

Deb, K. (2001): *Multi-objective Optimization Using Evolutionary Algorithms*. John Wiley & Sons.

Denton, J. D. (1993): Loss mechanisms in turbomachines. *Journal of Turbomachinery*, vol. 115, pp. 621–656.

Dunham, J. (1995): Aerodynamic losses in turbomachines. AGARD 85th Symposium on "Loss Mechanisms and Unsteady Flows in Turbomachines", CP-571.

Gaiddon, A.; Knight, D. D.; Poloni, C. (2004): Multicriteria design optimization of a supersonic inlet based upon global missile performance. *Journal of Propulsion and Power*, vol. 20, no. 3, pp. 542–558.

Glover, F. (1999): *New Ideas in Optimization*, chapter 19, pp. 297–316. McGraw Hill, 1999.

Glover, F.; Laguna, M. (1997): *Tabu Search*. Kluwer Academic Publishers.

Goldberg, D. E. (1989): *Genetic Algorithms in Search, Optimization and Machine Learning*. Addison-Wesley Publishing Company.

Hajela, P. (1999): Nongradient methods in multidisciplinary design optimization – status and potential. *Journal of Aircraft*, vol. 36, no. 1, pp. 255–265.

Haller, B. R.; Walker, P. J.; Singh, G.; Inche, N. Z. (1997): Application of 3D computational fluid dynamics methods to provide enhanced efficiency blading for the 21st century. pp. 61–80. 4th International Charles Parsons Turbine Conference.

Harvey, S. A. (2002): *The Design Optimisation of Turbomachinery Blade Rows*. PhD thesis, University of Cambridge, Department of Engineering, 2002.

Harvey, S. A.; Dawes, W. N.; Gallimore, S. J. (2003): An automatic design optimisation system for axial compressors part I: Software development. ASME GT2003-38115.

Hooke, R.; Jeeves, T. (1961): Direct search solution of numerical and statistical problems. *Journal of the ACM*, vol. 8, pp. 212–229.

Inselberg, A. (1985): The plane with parallel coordinates. *Visual Computer*, vol. 1, pp. 69–97.

Jaeggi, D. M.; Asselin-Miller, C.; Parks, G. T.; Kipouros, T.; Bell, T.; Clarkson, P. J. (2004): Multi-objective parallel Tabu Search. *Lecture Notes in Computer Science*, vol. 3242, pp. 732–741.

Jaeggi, D. M.; Parks, G. T.; Kipouros, T.; Clarkson, P. J. (2005): A multi-objective Tabu Search algorithm for constrained optimisation problems. *Lecture Notes in Computer Science*, vol. 3410, pp. 490–504.

Jaeggi, D. M.; Parks, G. T.; Kipouros, T.; Clarkson, P. J. (2006): The development of a multi-objective Tabu Search algorithm for continuous optimisation problems. *European Journal of Operational Research*, vol. feature issue on Adaptation of Discrete Metaheuristics for Continuous Optimization.

Jimenez-Octavio, J. R.; Lopez-Garcia, O.; Pilo, E.; Carnicero, A. (2008): Coupled electromechanical optimization of power transmission lines. *CMES: Computer Modeling in Engineering & Sciences*, vol. 25, no. 2, pp. 81–97.

Keane, A. J.; Nair, P. B. (2005): *Computational Approaches for Aerospace Design: The Pursuit of Excellence*. John Wiley & Sons.

Kipouros, T. (2006): *Multi-objective Aerodynamic Design Optimisation*. PhD thesis, Cambridge University, Department of Engineering, 2006. http://www-edc.eng.cam.ac.uk/˜tk291/kipouros-thesis.pdf.

Kipouros, T.; Ghisu, T.; Parks, G. T.; Savill, A. M. (2008): Using post-analyses of optimisation design processes as an active computational design tool. *ICCES*, vol. 335, no. 1, pp. 1–7.

Kipouros, T.; Jaeggi, D. M.; Dawes, W. N.; Parks, G. T.; Savill, A. M. (2005): Multi-criteria optimisation of turbomachinery blades: Investigating the trade-off surface. AIAA-2005-4023.

Kipouros, T.; Jaeggi, D. M.; Dawes, W. N.; Parks, G. T.; Savill, A. M. (2005): Multi-objective optimisation of turbomachinery blades using Tabu Search. *Lecture Notes in Computer Science*, vol. 3410, pp. 897–910.

Kipouros, T.; Jaeggi, D. M.; Dawes, W. N.; Parks, G. T.; Savill, A. M.; Clarkson, P. J. (2008): Biobjective design optimization for axial compressors using tabu search. *AIAA Journal*, vol. 46, no. 3, pp. 701–711.

Kipouros, T.; Mleczko, M.; Savill, A. M. (2008): Use of parallel coordinates for post-analyses of multi-objective aerodynamic design optimisation in turbomachinery. AIAA 2008-2138.

Kipouros, T.; Parks, G. T.; Savill, A. M.; Jaeggi, D. M. (2004): Multi-objective aerodynamic design optimisation. On CDRom Paper ERCODO2004_239.

Kirkpatrick, S.; Gelatt, C. D.; Vecchi, M. P. (1983): Optimization by simulated annealing. *Science*, vol. 220, no. 4598, pp. 671–680.

Kroo, I. (2004): Innovations in aeronautics. AIAA-2004-0001.

Lian, Y. S.; Liou, M. S. (2005): Mining of data from evolutionary algorithms for improving design optimization. *CMES: Computer Modeling in Engineering & Sciences*, vol. 8, no. 1, pp. 61–72.

Molinari, M.; Dawes, W. N. (2006): Review of evolution of compressor design process and future perspectives. *Proceedings of the Institution of Mechanical Engineers, Part C: Journal of Mechanical Engineering Science*, vol. 220, no. 6, pp. 761–771.

Molinari, M.; Jarrett, J. P.; Clarkson, P. J.; Dawes, W. N. (2006): Characterising the design space in multiobjective axial compressor blade optimisation. AIAA-2006-1908.

Morino, L.; Bernardini, G.; Mastroddi, F. (2006): Multi-disciplinary optimization for the conceptual design of innovative aircraft configurations. *CMES: Computer Modeling in Engineering & Sciences*, vol. 13, no. 1, pp. 1–18.

Nemec, M.; Zingg, D. W.; Pulliam, T. H. (2004): Multipoint and multi-objective aerodynamic shape optimization. *AIAA Journal*, vol. 42, no. 6, pp. 1057–1065.

Rogers, D. F. (2000): *An Introduction to NURBS with Historical Perspective*. Morgan Kaufmann Publishers.

Sasaki, D.; Obayashi, S.; Nakahashi, K. (2002): Navier-Stokes optimization of supersonic wings with

four objectives using evolutionary algorithm. *Journal of Aircraft*, vol. 39, no. 4, pp. 621–629.

Snir, M.; Otto, S.; Huss-Lederman, S.; Walker, D.; Dongarra, J. (1998): *MPI: The Complete Reference*. The MIT Press.

Storer, J. A.; Cumpsty, N. A. (1991): Tip leakage flow in axial compressors. *Journal of Turbomachinery*, vol. 113, pp. 252–259.

Vanderplaats, G. N. (2001): Design optimization – a powerful tool for the competitive edge. AIAA-2001-5214.

Zhu, Z. Q.; Liu, Z.; Wang, X. L.; Yu, R. X. (2004): Construction of integral objective function/fitness function of multi-objective/multi-disciplinary optimization. *CMES: Computer Modeling in Engineering & Sciences*, vol. 6, no. 6, pp. 567–576.



https://dspace.org/

Insight into high-quality aerodynamic design spaces through multi-objective optimization

Kipouros, Timoleon; Jaeggi, Daniel; Dawes, Bill; Parks, Geoff; Savill, Mark A. ...

2008-01-01T00:00:00Z
Tech Science Press
http://dspace.lib.cranfield.ac.uk/handle/1826/4386
Kipouros T, Jaeggi DM, Dawes WN, et al., (2008) Insight into high-quality aerodynamic design spaces through multi-objective optimization. CMES: Computer Modeling in Engineering and Sciences, 2008, Volume 37, Issue 1, pp 1-23

Downloaded from a DSpace repository. https://dspace.org/